Clay nanosheets simultaneously intercalated and stabilized by PEGylated chitosan as drug delivery vehicles for cancer chemotherapy

Hsuan-Jung Huang [a], Shih-Yu Huang [a], Tzu-Hao Wang [a], Tzu-Yun Lin [a], Nan-Ching Huang [a], Orion Shih [b], U-Ser Jeng [b], Che-Yi Chu [a,*], Wen-Hsuan Chiang [a,*]

[a] Department of Chemical Engineering, National Chung Hsing University, Taichung 402, Taiwan
[b] National Synchrotron Radiation Research Center, Hsinchu 30076, Taiwan

ARTICLE INFO

ABSTRACT

Montmorillonite (MMT) has been frequently utilized as drug vehicles due to its high specific surface area, excellent cation exchange capacity and biocompatibility. However, the significant flocculation of MMT under physiological condition restricted its application to drug delivery. To conquer this problem, the graft-type PEGylated chitosan (PEG-CS) adducts were synthesized as intercalator to stabilize MMT dispersion. Through electrostatic attraction between the chitosan and MMT, the PEG-CS adducts were adsorbed on MMT surfaces and intercalated into MMT. The resulting PEG-CS/MMT nanosheets possessed PEG-rich surfaces, thus showing outstanding dispersion in serum-containing environment. Moreover, the physicochemical characterization revealed that the increased mass ratio of PEG-CS to MMT led to the microstructure transition of PEG-CS/MMT nanosheets from multilayered to exfoliated structure. Interestingly, the PEG-CS/MMT nanosheets with mass ratio of 8.0 in freeze-dried state exhibited a hierarchical lamellar structure organized by the intercalated MMT bundles and unintercalated PEG-CS domains. Notably, the multilayered PEG-CS/MMT nanosheets showed the capability of loading doxorubicin (DOX) superior to the exfoliated counterparts. Importantly, the DOX@PEG-CS/MMT nanosheets endocytosed by TRAMP-C1 cells liberated the drug progressively within acidic organelles, thereby eliciting cell apoptosis. This work provides a new strategy of achieving the controllable dispersion stability of MMT nanoclays towards application potentials in drug delivery.

1. Introduction

Aim at promoting potency of the cancer treatment with reducing side effect by the effective tumor accumulation of chemotherapy drugs via the innate enhanced permeability and retention (EPR) effect of solid tumors, various organic nanoparticles including liposomes, polymeric micelles, and solid-lipid nanoparticles have been extensively utilized as drug carriers in the past two decades (Dang & Guan, 2020; Hsieh et al., 2022; Mitchell et al., 2021). Some of them have further been approved by the Food and Drug Administration (FDA), USA, and adopted in clinical cancer treatment, known as Doxil (PEGylated liposomal doxorubicin), Abraxane (paclitaxel-bound albumin), DepoCyt (liposomal cytarabine), and Genexol-PM (polymeric micelle formulation) (Lee et al., 2008; Yalamandala et al., 2021). Furthermore, a variety of inorganic nanoscale clay minerals (such as halloysite, layered double hydroxide, and montmorillonite) to be used as drug delivery systems have also attracted substantial attention owing to their high porosity, large

specific surface area, excellent biocompatibility, good thermal and chemical stability, and availability in diffusion-controlled drug release mechanism (Jafarbeglou et al., 2016; Khatoon et al., 2020; Peixoto et al., 2021). Among these clay minerals, montmorillonite (abbreviated as MMT) is one of the most abundant smectite clays, which is composed of aluminosilicate layers with the dimension of ca. $100 \times 100 \times 1$ nm^3 in each plate piling in a primary stack of ca. 8–10 layers through massive charge attraction (Chen et al., 2008). The negative charge ($\cong 76$ meq/100 g) of MMT nanoclays derived from isomorphic substitutions between Al^{3+} and Si^{4+} can be naturally compensated by inorganic cations (Kohay et al., 2017). Additionally, the unique layered structure of MMT stabilizes the bioactive molecules through electrostatic interaction for applications to drug release in a well-controlled manner by exchanging the bioactive molecules with other ions existing in the biological system (Bekaroğlu et al., 2018; Chen et al., 2008; Kohay et al., 2017). However, despite the aforementioned advantages of MMT, either the significant flocculation and precipitation of MMT under physiological condition

due to the high salt concentration and the presence of proteins or the incomplete drug release from MMT-drug formulations would still largely restrict its EPR effect-based drug delivery (Joshi et al., 2009; Kohay et al., 2017).

In order to tackle the problems mentioned above, several strategies of integrating the clay nanoparticles with functionalized organic materials to form organic-inorganic nanohybrids as drug delivery systems have been reported (Akbal et al., 2018; Iliescu et al., 2014; Kohay et al., 2017; Li et al., 2016; Sreekanth Reddy et al., 2021; Takahashi et al., 2005). For example, as pioneers, Takahashi et al. considered the use of (α-acetal-poly(ethylene glycol)-*block*-[poly(2-(*N*,*N*-dimethylamino) ethyl methacrylate)] (Acetal-PEG-*b*-PAMA) to modify clay surfaces (Takahashi et al., 2005), through which the electrostatic attraction between the negative charges from clay surfaces and the positive charges from cationic PAMA segments in Acetal-PEG-*b*-PAMA allowed the hydrophilic PEG brush layers to effectively cover clay surfaces for enhancing the dispersion stability of the Acetal-PEG-*b*-PAMA/clay nanohybrids in aqueous solutions of high ionic strength; in this case, the hydrophobic pyrene molecules that were subsequently incorporated into nanopores of the nanohybrids were able to release sustainably. Furthermore, as reported by Kohay et al. (Kohay et al., 2017), to realize the efficient intracellular delivery of doxorubicin (DOX), a chemotherapy drug, the DOX-encapsulated polymeric micelles composed of poly(ethylene glycol)-phosphatidylethanolamine (PEG-PE) were treated by adsorption onto the MMT, so that the DOX-loaded PEG-PE/MMT nanocomposites exhibited the appreciably promoted in vitro drug release and cytotoxicity against the DOX-resistant MCF-7 cells with compared to the case of DOX-carrying MMT. Moreover, Sreekanth Reddy et al. developed the dual cross-linked sodium alginate (SA)/MMT nanohybrid beads as a vehicle for the extended release of curcumin (Sreekanth Reddy et al., 2021); this type of nanohybrid beads displayed a higher degree of swelling at pH 7.4 than at pH 1.2, thus accelerating release of curcumin even it has initially been intercalated within MMT. The instances given above showed application potentials of the organic-inorganic MMT nanohybrids as drug carriers, whereas the impact of the intercalation of incorporated polymers on the drug release mechanisms of the MMT-based nanohybrids still remains unclear. On the other hand, to the best of our knowledge, most of MMT-based nanohybrids used as
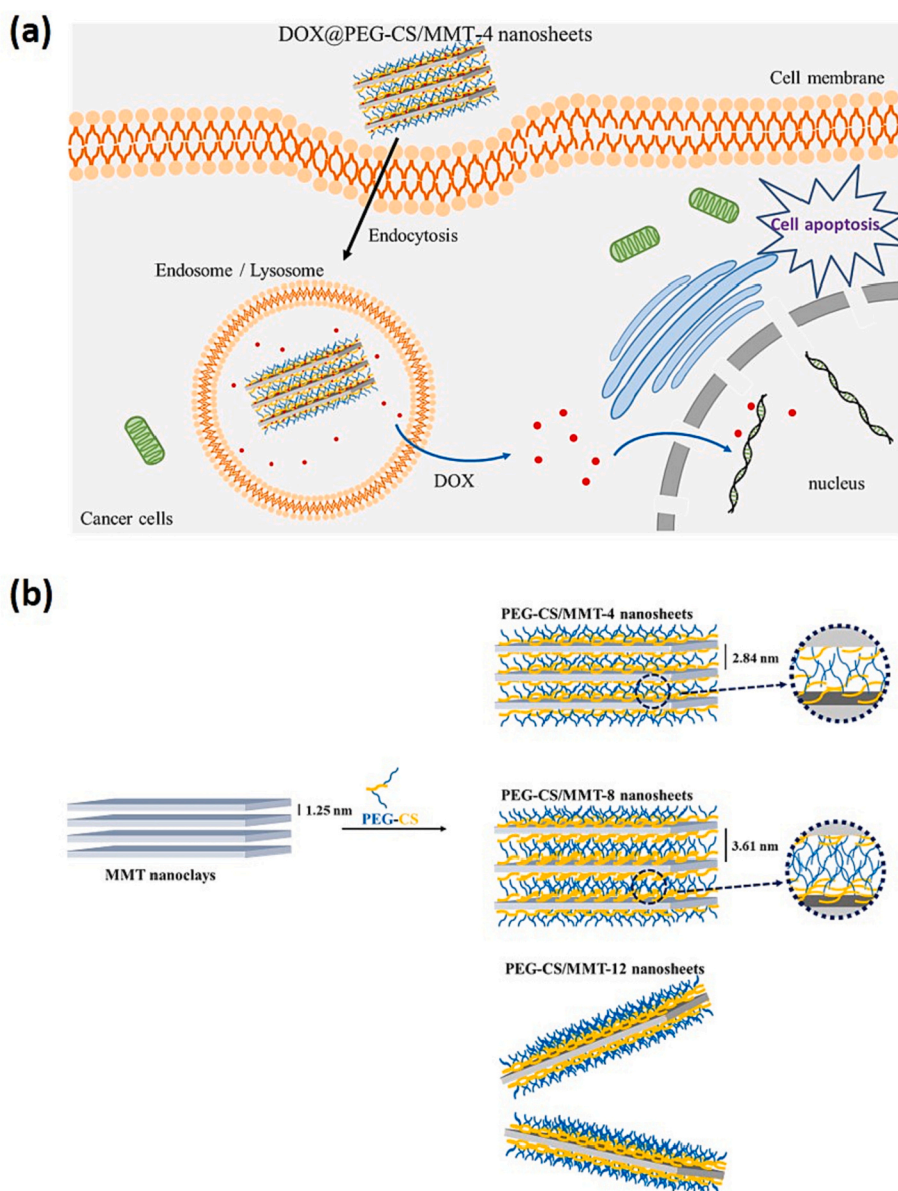
Scheme 1. Schematic illustrations of (a) DOX@PEG-CS/MMT nanosheets for the intracellular drug delivery and cancer chemotherapy and (b) the changes in microstructures of PEG-CS/MMT nanosheets with various PEG-CS/MMT mass ratios.

drug vehicles were often fabricated by intercalation/adsorption of MMT with linear homopolymers or block copolymers (Anirudhan & Parvathy, 2018; Iliescu et al., 2014; Kohay et al., 2017; Murugesan & Scheibel, 2020; Takahashi et al., 2005); contrarily, the study on the nanohybrids formed by intercalation of MMT with graft-type copolymers is still limited, where the grafted molecules could however offer extra functionality as will be discussed in this study.

In the current study, we synthesize the PEGylated chitosan (abbreviated as PEG-CS) graft-type adducts as an intercalator and stabilizer for MMT nanoclays to subsequently prepare the PEG-CS/MMT nanosheets as a kind of DOX-carrying vehicles for the intracellular DOX delivery and cancer chemotherapy, as illustrated in Scheme 1a. The PEG coating on the surfaces of nanoparticles has been demonstrated to be able to effectively reduce their elimination by the reticuloendothelial system (RES), thereby prolonging their blood circulation time to enhance accumulation in the tumor by the EPR effect (Guo & Huang, 2011; Hoang Thi et al., 2020). Thus, we further applied the grafting of PEG in chitosan as a strategy to accumulate the PEG-CS/MMT nanosheets in the tumor in a similar manner. Chitosan is a biodegradable polysaccharide of N-acetylglucosamine and D-glucosamine, which has been commonly utilized in the biomedical field (Ding et al., 2019; Huang et al., 2022). It has been reported that chitosan can exchange the interlayer cations of clay by an ion exchange process (Altunkaynak et al., 2022; de Lima et al., 2022; Monvisade & Siriphannon, 2009; Tavares et al., 2022; Yuan et al., 2010); consequently, through the electrostatic attraction between the positive NH_3^+ groups of chitosan and the negatively charged sites of clay, chitosan can be adsorbed on clay surfaces and/or intercalated into the layered structure of clay (Monvisade & Siriphannon, 2009; Yuan et al., 2010). As a result, it was reasonably speculated that the grafted hydrophilic PEG segments could be decorated on the outer surfaces of the PEG-CS/MMT nanosheets mediated by the electrostatic attraction between chitosan and MMT as illustrated in Scheme 1b, thereby stabilizing the dispersion of PEG-CS/MMT nanosheets in serum-containing aqueous solutions of high ionic strength in this study. To further investigate the effect of mass ratio of PEG-CS to MMT nanoclays in feed on the resultant microstructure and the corresponding DOX loading of PEG-CS/MMT nanosheets, the morphologies including the primary particle size, self-assembled structure, and basal spacing of nanosheets were characterized by using static/dynamic light scattering (SLS/DLS), X-ray diffraction (XRD), and small-angle X-ray scattering (SAXS) coupled with transmission electron microscope (TEM), scanning electron microscope (SEM), and atomic force microscope (AFM). In addition, the in vitro DOX release from PEG-CS/MMT nanosheets under different pH conditions and in the presence of glutathione (GSH) was also explored. The in vitro cellular uptake of DOX-loaded PEG-CS/MMT nanosheets by TRAMP-C1 cells and their cytotoxicity were evaluated as well.

2. Experimental section

2.1. Materials

MMT (purity >98 %), polyethylene glycol monomethylether (mPEG) (M.W. = 5 kDa), N-hydroxysuccinimide (NHS, 98 %) and 3-(4,5-dimethylthiazol-2-yl)-2,5-diphenyltetrazolium bromide (MTT, purity >98 %) were purchased from Alfa Aesar (USA). N-(3-dimethylaminopropyl)-N′-ethylcarbodiimide hydrochloride (EDC, 95 %) was attained from Matrix Scientific (USA). Chitosan (M.W. = 5 kDa, 81 % degree of deacetylation) was obtained from Glentham Life Science Ltd. (UK). DOX hydrochloride was obtained from Carbosynth Ltd. (UK). Hoechst 33342 was purchased from Invitrogen (USA). Dulbecco's modified Eagle medium (DMEM), trypsin-EDTA and D_2O (99.9 atom% D) were purchased from Sigma Aldrich (USA). Fetal bovine serum (FBS) was obtained from Hyclone (USA). TRAMP-C1 cells (murine prostate cancer cell line) were attained from Food Industry Research and Development Institute (Hsinchu city, Taiwan).

2.2. Size reduction of MMT nanoclays

In order to improve the medical application of MMT nanoclays, the particle size was reduced by the following approach. Na^+-MMT (20 mg) dispersed in deionized water (2.0 mL) was sonicated (at a frequency of 20 kHz and a power of 6 W) with probe-type sonicator (Sonicator®3000, MISONIX) under ice-water condition for 10 min (60 s on and 30 s off). The sonicated solution containing MMT nanoclays was stored at 4 °C.

2.3. Synthesis and characterization of PEG-CS graft-type adducts

The mPEG-COOH utilized in this study were synthesized and characterized according to the procedure reported previously (Hsu et al., 2020). The PEG-CS adducts were prepared by the EDC/NHS-mediated amindation of chitosan and mPEG-COOH as shown in Scheme S1 of the Supporting Information. Briefly, mPEG-COOH (295 mg), NHS (136 mg), and EDC (227 mg) were dissolved in deionized water (7.0 mL), and subsequently, the chitosan (100 mg) dissolved in deionized water was added dropwise into the former solution and stirred at 25 °C for 48 h, followed by dialysis (Cellu Sep MWCO 6000–8000) against deionized water to eliminate NHS and EDC. Then, the PEG-CS adducts were obtained by lyophilisation and characterized by Fourier transform infrared (FT-IR) spectroscopy (FT-720, HORIBA, Japan) and proton nuclear magnetic resonance (^1H NMR) spectroscopy (Agilent DD2 600 MHz NMR spectrometer) as shown in Figs. 1c and 2c, respectively.

2.4. Preparation of PEG-CS/MMT nanosheets and DOX@PEG-CS/MMT nanosheets

The PEG-CS/MMT nanosheets with various mass ratios of PEG-CS to MMT in feed were attained by one-step process. For example, the PEG-CS/MMT nanosheets with a PEG-CS/MMT mass ratio of 4.0 (which was named as PEG-CS/MMT-4) were prepared by adding the sonicated MMT nanoclays (1.0 mg) into deionized water (1600 μL) under stirring to obtain the MMT-containing solution; subsequently, 4.0 mg PEG-CS adducts dissolved in deionized water (400 μL) was added dropwise to the MMT-containing solution under stirring to yield the mixture of PEG-CS and MMT in deionized water. The mixed solution was further stirred at 50 °C for 24 h and then dialyzed (MWCO 6000–8000 Da) with phosphate buffer (pH 7.4, 0.01 M) at 4 °C for 24 h to obtain the PEG-CS/MMT-4 nanosheets. Similarly, the nanosheets of CS/MMT, and PEG-CS/MMT-2, PEG-CS/MMT-8 and PEG-CS/MMT-12 with the PEG-CS/MMT mass ratios equal to 2, 8 and 12, respectively, were prepared in the similar manner.

For the preparation of the DOX@PEG-CS/MMT-4 nanosheets, DOX hydrochloride dissolved in dimethyl sulfoxide (DMSO) (1.5 mg/mL, 0.2 mL) was added dropwise into the aqueous solution of MMT nanoclays (1.0 mg, 1400 μL) and stirred at room temperature for 2 h; afterward, PEG-CS adducts (4.0 mg) dissolved in deionized water (400 μL) were added into the DOX/MMT aqueous solution and stirred at 50 °C for 24 h. It has been reported that the electrostatic attraction of positively-charged DOX molecules with negatively-charged macromolecules cannot be declined until the ionic strength of the solution exceeded 0.1 M, which would thus accelerate DOX liberation (Lanz-Landázuri et al., 2014; Manocha & Margaritis, 2010). Based on the previous studies, to prevent the undesirable leakage of DOX molecules loaded within nanosheets during purification process in this work, the as-prepared DOX@PEG-CS/MMT-4 nanosheets suspension was dialyzed (MWCO 6000–8000 Da) with phosphate buffer at 0.01 M and pH 8.0 at 4 °C for 24 h to completely remove the unloaded DOX and the DMSO solvent. For comparison, the DOX@MMT nanoclays without hybridizing PEG-CS and the DOX@PEG-CS/MMT-8 nanosheets were prepared by means of the similar procedure.
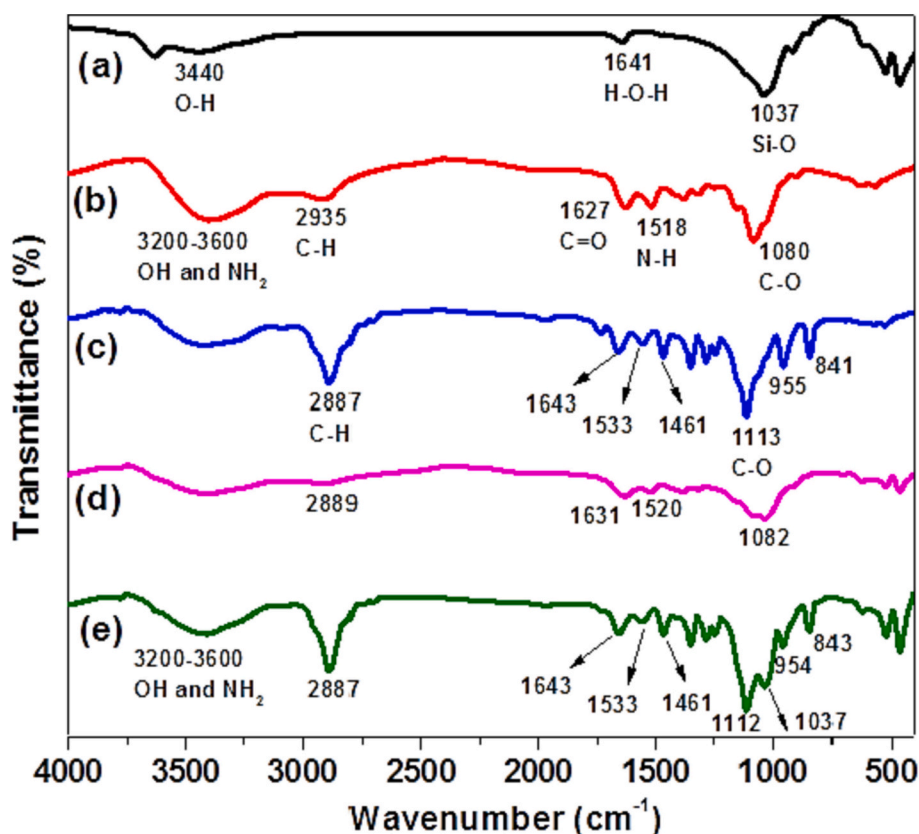
Fig. 1. FT-IR spectra of (a) MMT nanoclays, (b) chitosan segments, (c) PEG-CS adducts, (d) CS/MMT nanosheets, and (e) PEG-CS/MMT-4 nanosheets.
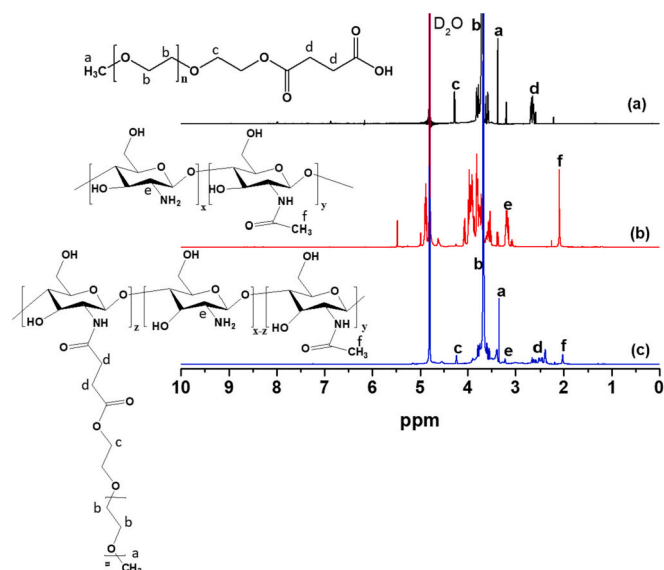

Fig. 2. ^{1}H NMR spectra of (a) mPEG-COOH, (b) chitosan segments, and (c) PEG-CS adducts.

2.5. Structural characterization of the MMT-based nanosheets and determination of the drug loading capacity

The chemical structure of the MMT nanoclays and the PEG-CS/MMT nanosheets was characterized by a HORIBA FT-720 FT-IR spectroscopy. FT-IR spectra were collected in the wavenumber range of 4000–400 cm^{-1} with a resolution of 4 cm^{-1} and 32 scans for each sample. Thermogravimetric analysis (TGA) was conducted with a Thermo Scientific Cahn TGA Versa Therm-HS under an N_2 atmosphere by heating the sample to 800 °C at the rate of 10 °C/min to study the weight ratios of each component in the nanosheets. The zeta potential of MMT nanoclays and its hybridization with PEG-CS in aqueous solutions was measured by an Anton Paar Litesizer 500. At least triplicate measurements of each sample were conducted and then averaged.

The mean hydrodynamic diameter (D_h) of MMT nanoclays and PEG-CS/MMT nanosheets in aqueous solutions was determined by DLS using a Brookhaven BI-200SM goniometer equipped with a BI-9000 AT digital correlator and with a solid-state laser (35 mW, $\lambda = 637$ nm) detected at a scattering angle of 90°. The root-mean-square radius of gyration (R_g) of PEG-CS/MMT nanosheets was determined according to the Berry plot of the scattering intensity ($I_{ex}^{-1/2}$) versus the square of the scattering vector (q^2). The ratio of R_g to the mean hydrodynamic radius (R_h) was explored with the angular dependent DLS/SLS measurements. Furthermore, XRD measurements were performed using a D8 Discover X-ray diffractometer (Bruker, Germany) with CuKα radiation (40 kV, $\lambda = 0.15$ nm) at a scan rate of 2°/min to obtain the basal spacing of MMT nanoclays, CS/MMT nanosheets, and PEG-CS/MMT nanosheets by the Bragg's law. Moreover, the larger length-scale structure associated with the self-assembly of clay bundles in the freeze-dried PEG-CS/MMT nanosheets was probed by SAXS performed at the Endstation TPS 13A1 of the National Synchrotron Radiation Research Center (NSRRC), Taiwan. The energy of the X-ray source and the sample-to-detector distance were 6 keV and 10,414.1 mm, respectively. The scattering signals were collected using an in-vacuum Eiger X 9 M detector with a typical exposure time of 30 s. The one-dimensional (1-D) scattering intensity profile was output as a plot of the scattering intensity (I) versus the magnitude of the scattering vectors, $q = (4\pi/\lambda) \sin (\theta/2)$ (θ = scattering angle). The SAXS profiles were corrected for the incident beam intensity, the detector sensitivity, and the background.

The real-space images of the morphology of MMT nanoclays and PEG-CS/MMT nanosheets were collected using TEM (JEM-1400Flash

Electron Microscope, JEOL, Japan), SEM (UltraPlus, Zeiss, Germany), and AFM (FSM Nanoview1000, China). The samples used for TEM study were prepared by placing a few drops of MMT nanoparticle solution or PEG-CS/MMT nanosheet solutions on the 300-mesh copper grids coated with carbon film and followed by drying at 25 °C for 2 days before measurements. The samples used for SEM study were prepared by dropping 5 μL of MMT nanoparticle solution or PEG-CS/MMT nanosheet solutions onto the silicon substrates with a low specific resistivity of 0.011–0.012 Ωcm followed by air dry, and then were sputtered with platinum. For the AFM image acquisition, the MMT nanoclay solution and the PEG-CS/MMT nanosheet solutions were spin-coated on the surfaces of the silicon wafers for subsequent measurements.

To determine the drug loading capacity, a small portion of DOX@MMT nanoclays or DOX@PEG-CS/MMT nanosheets was lyophilized and then dispersed in DMSO to extract the DOX. The amount of DOX extracted was quantitatively determined by a fluorescence spectrophotometer (Hitachi F-2700). The excitation was performed at 480 nm and the emission spectrum was recorded in the range of 500–700 nm. The calibration curve used for the drug loading characterization was established by using the fluorescence intensities of DOX at various concentrations in DMSO. Drug loading efficiency (DLE) and drug loading content (DLC) were respectively calculated based on the following formulas:

$$\text{DLE (\%)} = (\text{weight of loaded DOX/weight of DOX in feed}) \times 100\% \quad (1)$$

$$\begin{aligned}\text{DLC (\%)} = &(\text{weight of loaded DOX/weight of DOX} \\ &- \text{containing formulations}) \times 100\%\end{aligned} \quad (2)$$

2.6. Stimuli-triggered drug liberation

The drug release profiles at different pH values were determined by the dialysis technique. 1.0 mL DOX@PEG-CS/MMT-4 nanosheet solution was placed within a dialysis tube (Cellu Sep MWCO 6000–8000), followed by dialysis against the different buffer solutions (e.g., acetate buffer of pH 5.0 or phosphate buffer saline (PBS) of pH 7.4 at 20 mL with ionic strength of 0.15 M) at 37 °C. At prescribed time intervals, 1.0 mL external buffer solution was withdrawn and replaced with an equivalent volume of fresh medium. The concentration of DOX was determined by the fluorescence technique using the pertinent calibration curve of DOX with various concentrations in buffer solution of either pH 5.0 or 7.4. The experimental results presented herein represented an average of at least triplicate measurements. To explore the effect of GSH on DOX liberation from DOX@PEG-CS/MMT nanosheets, the DOX fluorescence intensity of DOX@PEG-CS/MMT nanosheets dispersed in PBS containing 10.0 mM GSH was measured by a fluorescence spectrophotometer (Hitachi F-2700) at different time intervals.

2.7. In vitro cellular uptake

TRAMP-C1 cells (2×10^5 cells/well) seeded in a 6-well plate containing 22 mm round glass coverslips were cultured overnight. The cells were then respectively incubated with free DOX molecules and DOX@PEG-CS/MMT-4 nanosheets (DOX concentration = 10 μM) at 37 °C for 1 h and 4 h. Upon washing twice with PBS and fixing with 4 % formaldehyde, the cells were stained with Hoechst 33342 for 5 min, and the slides were rinsed three times with PBS. Coverslips were placed onto the glass microscope slides, and the cellular images were acquired at the excitation wavelengths of 405 and 488 nm for Hoechst and DOX, respectively, by a confocal laser scanning microscope (CLSM) (Olympus, FluoView FV3000, Japan).

2.8. In vitro cytotoxicity study

TRAMP-C1 cells seeded in a 96-well plate at a density of 1×10^4 cells/well were incubated in DMEM (100 μL) containing 10 % FBS and 1

% penicillin at 37 °C for 24 h. The culture medium was then replaced with 100 μL fresh medium containing either MMT nanoclays, PEG-CS/MMT-4 nanosheets, free DOX molecules or DOX@PEG-CS/MMT-4 nanosheets with various DOX concentrations, and then the cells were incubated at 37 °C for additional 24 h. Subsequently, 100 μL MTT (0.25 mg/mL) was added into each well followed by incubation at 37 °C for 3 h. After the removal of the culture medium, DMSO was added to dissolve the precipitate, and the absorbance at 570 nm of the resulting solution was measured by using a BioTek 800TS microplate reader.

3. Results and discussion

3.1. Structural characterization of PEG-CS/MMT nanosheets

The PEG-CS adducts utilized as intercalator and stabilizer for MMT nanoclays was synthesized by the conjugation of chitosan with mPEG-COOH via the EDC/NHS-mediated amindation reaction. In comparison to the pure chitosan (Fig. 1b), the FT-IR spectrum of PEG-CS adducts shown in Fig. 1c revealed the absorption bands at 1113 and 955/841 cm^{-1} for the C—O and C—C stretching vibrations of mPEG segments, and at 1643, 1533 and 1461 cm^{-1} for the C=O, N—H and C—N stretching vibrations of amide groups, respectively, signifying the successful modification of chitosan with mPEG-COOH. Furthermore, the characteristic feature of the proton signals of mPEG-COOH at δ 3.7 and 3.4 ppm and that of chitosan at δ 3.5–4.0, 3.2 and 2.0 ppm were observed in the ^{1}H NMR spectrum of the synthesized PEG-CS adducts, as displayed in Fig. 2. According to the integral ratio of the signals of the methoxy protons from mPEG-COOH at δ 3.4 ppm to the acetyl protons from chitosan at δ 2.0 ppm, the degree of the substitution of chitosan with mPEG-COOH defined as the number of mPEG segments per 100 glucosamine units was attainted to be ca. 9.4.

On the other hand, the average size of commercial MMT clays was up to 1–2 μm due to particle aggregation (Kohay et al., 2017) and cannot be directly applied to the tumor-targeted drug delivery based on the EPR effect. To overcome this hurdle, the commercial MMT clays have further been treated with probe-type sonication for a reduction in the average size. As indicated by the black profile shown in Fig. S1, the particle size of the sonicated MMT nanoclays in deionized water was successfully reduced to ca. 333 nm upon sonication as determined by DLS. However, once the sonicated MMT nanoclays were dispersed in the 0.15 M PBS of high salt concentration at pH 7.4, particle aggregation occurred again as manifested by the appreciably enlarged particle size (increased to ca. 447 nm) as shown in Fig. 3a. Such a flocculation of MMT nanoclays at the salt concentration higher than 0.1 M could be ascribed to that their surface charges have been largely shielded by salt ions as reported by Nagasaki et al.[13] Previous studies reported that the dispersion stability of nanoclays can be considerably enhanced by surface modification with the hydrophilic PEG (Jermy et al., 2022; Takahashi et al., 2005) or by the intercalation of cationic chitosan in the interpolate space between the silicate layers of clay via an ion exchange process (Mokhtar et al., 2018; Monvisade & Siriphannon, 2009; Yuan et al., 2010). Consequently, we attempted to develop a unique PEG-CS/MMT nanosheet system by hybridizing the as-synthesized PEG-CS adducts (with the combination of properties from both the mPEG and chitosan) as intercalator to stabilize the MMT clay suspension; furthermore, a series of PEG-CS/MMT nanosheets with the different prescribed mass ratios of PEG-CS to MMT in feed were prepared for examining the crucial effect of the incorporated amount of PEG-CS on its ability to stabilize the MMT nanoclays. It can be seen in Fig. S1 of the Support Information that the particle size of PEG-CS/MMT nanosheets in deionized water was indeed reduced remarkably from 333 to 241 nm when the PEG-CS/MMT mass ratio was increased from 0 to 8.0. This trend was held even after transferring the nanosheet samples to the medium with a higher salt concentration of 0.15 M PBS, as shown in Fig. 3a; in other words, the MMT nanoclays and PEG-CS/MMT-2 nanosheets showed the larger particle sizes with diluted by 0.15 M PBS, whereas both of the PEG-CS/
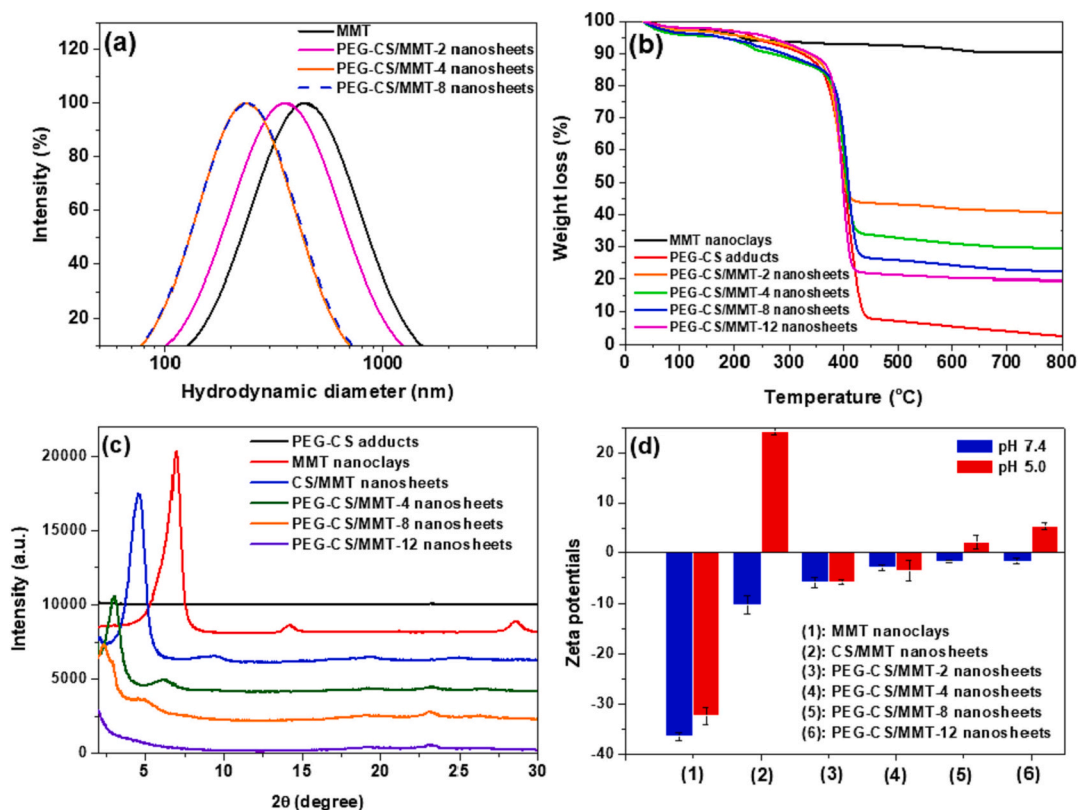
Fig. 3. (a) DLS profiles of the MMT nanoclays and PEG-CS/MMT nanosheets dispersed in PBS of pH 7.4. (b) TGA curves of the MMT nanoclays, PEG-CS adducts, and PEG-CS/MMT nanosheets. (c) XRD profiles of the MMT nanoclays, PEG-CS adducts, CS/MMT nanosheets, and PEG-CS/MMT nanosheets. (d) Zeta potential of the MMT nanoclays, CS/MMT nanosheets, and PEG-CS/MMT nanosheets dispersed in the aqueous solutions of pH 7.4 or 5.0.

MMT-4 and PEG-CS/MMT-8 nanosheets were found to keep the smaller particle sizes comparable to their counterparts in deionized water. This thus evidenced that the incorporation of adequate amount of PEG-CS adducts bearing the hydrophilic PEG segments was beneficial to the enhancement of the dispersion stability of MMT nanoclays in an aqueous solution of physiological salt concentration.

To further examine if the hybridization of MMT nanoclays and PEG-CS adducts was successfully achieved, firstly, the FT-IR spectrum of PEG-CS/MMT nanosheets was acquired as shown in Fig. 1e (here the representative PEG-CS/MMT-4 nanosheet sample was selected for FT-IR study). In addition to the presence of the absorption band at 1037 cm^{-1} for Si—O stretching vibration from MMT, the absorption bands at 1643, 1533, 1466, 1112, 954 and 843 cm^{-1} contributed from PEG-CS were also observed in the FT-IR spectrum. Moreover, the TGA analysis displayed in Fig. 3b indicated that the weight losses of the PEG-CS adducts in PEG-CS/MMT-2, PEG-CS/MMT-4, PEG-CS/MMT-8, and PEG-CS/MMT-12 nanosheets were 60.5, 70.4, 76.5, and 81.0 %, respectively, corresponding to the tendency of the increased amount of PEG-CS adducts being added in these PEG-CS/MMT nanosheet samples. The FT-IR and TGA results confirmed that the PEG-CS was properly incorporated into MMT by the ion exchange-mediated hybridization of chitosan segments.

To gain an insight into the local structure associated with the stacking of clay platelets in the different PEG-CS/MMT nanosheets, XRD experiment was performed and the results are shown in Fig. 3c. As compared to the pristine MMT nanoclays showing a remarkable diffraction peak at 6.9°, the diffraction found for the CS/MMT nanosheets shifted to 4.9°, signifying that the intercalation of chitosan could expand the inter-clay distance between clay platelets in MMT from 1.25 to 1.9 nm as calculated by the Bragg's law; the similar finding has been reported by Misra's group (Yuan et al., 2010). Notably, when the PEG-CS was used to replace chitosan as in the case of PEG-CS/MMT-4

nanosheets, the diffraction peak significantly shifted to much lower reflection angle at 3.2° as the inter-clay distance of MMT was greatly enlarged to 2.84 nm by the intercalation of PEG-CS adducts. With increasing the mass ratio of PEG-CS to MMT up to 8.0, the inter-clay distance of the resulting PEG-CS/MMT-8 nanosheets was further increased to 3.61 nm. Such an appreciable expansion of the inter-clay distance of PEG-CS/MMT nanosheets with hybridizing more PEG-CS adducts revealed that the ionic exchange of chitosan with the MMT surfaces coupled with the directed interaction of the oxygen from PEG with the exchangeable cations (ion-dipole) (Alemdar et al., 2005; Chiu et al., 2014; Kohay et al., 2017) could dominate the mechanisms of the inter-clay expansion. It is noted that the disappearance of the diffraction peak in the PEG-CS/MMT-12 nanosheets suggested that the incorporation of excessive PEG-CS adducts unavoidably led to the exfoliation of MMT nanoclays; the exfoliation of MMT driven by the incorporation of high amounts of polymer chains has also been reported elsewhere (Chiu et al., 2014).

The ionic association of chitosan or PEG-CS adducts on the surfaces of MMT layers was expected to be capable of shielding the surface charges of MMT. As presented in Fig. 3d, the zeta potential of MMT measured after being intercalated with chitosan in pH 7.4 aqueous solution was considerably changed from −36.4 (for the pristine MMT) to −10.2 mV, as the fact that the negatively-charged surfaces of the MMT nanoclays were at least partly covered by the positively-charged chitosan segments via electrostatic attraction, thus giving rise to a significant reduction in the zeta potential. This behavior was also attained for the PEG-CS/MMT nanosheets as can be seen from Fig. 3d. The similar behavior of the reduction of zeta potential has also been observed for the ionic association of positively-charged chitosan segments on the negatively-charged surfaces of the poly(e-caprolactone) nanocapsules carrying herbicide atrazine (Grillo et al., 2014). Interestingly, as the pH value in the same solutions was tuned to 5.0, the corresponding zeta

potential of CS/MMT nanosheets was dramatically converted from negative to positive value (=24 mV); this phenomenon was never found for the case of pristine MMT nanoclays as which showed the nearly unchanged zeta potential with compared to that obtained in pH 7.4. Such an acidity-elicited transition in zeta potential of CS/MMT nanosheets could be attributed to the enhanced protonation of the amine groups of chitosan segments in weak acidic milieu. As for the PEG-CS/MMT nanosheets, by contrast, the zeta potential could still be virtually retained in response to the pH reduction to 5.0. This result strongly implied that the outer PEG segments from PEG-CS that have been properly covered on the top of the MMT surfaces could largely shield the positive charges of the protonated chitosan segments.

On the basis of XRD and zeta potential studies, the self-organized microstructures of the PEG-CS/MMT nanosheets at different PEG-CS/MMT mass ratios can be rationally deduced. As a result, we proposed that the PEG-CS adducts could be intercalated into the MMT clay platelets of PEG-CS/MMT nanosheets, where the chitosan backbone interacted directly with the surfaces of MMT platelets to build up the inner chitosan layer and the outer layer composed of the grafted PEG brushes covered on the top of the chitosan layer, as schematically illustrated in Scheme 1b. It should be noted that the diffraction peak associated with the inter-clay stacking in both the cases of PEG-CS/MMT-4 and PEG-CS/MMT-8 nanosheets was sharp, suggesting that the stacking of the intercalated MMT clay platelets was in a long-range ordered state. It was because the samples of these two PEG-CS/MMT nanohybrids prepared for the XRD measurements were pretreated by dropping the hybrid solutions onto the silicon wafers followed by removal of the solvent at room temperature; under this condition, the MMT platelets easily stacked to a certain extent upon the solvent removal to minimize the total surface free energy. However, the well-ordered stacking of clay platelets would probably not be favorable to drug loading because the transport kinetics through such a constrained architecture could be slow.

Instead, the long-range stacking of intercalated MMT platelets upon solvent removal as concerned above was able to be inhibited by the freeze-drying process (i.e., by a low-temperature dehydration process

with removing the freezing aqueous solvent by sublimation) due to the kinetically-trapped effect. The SAXS profiles of the MMT nanoclays, PEG-CS/MMT-4 nanosheets, and PEG-CS/MMT-8 nanosheets treated by the freeze-drying process are shown in Fig. 4a to study the self-assembly behavior at nanometer scale, through which the inter-clay stacking of MMT platelets and the higher-level structures further organized by MMT clay bundles can be investigated. First, MMT nanoclays displayed no long-range ordered nanostructure as indicated by the absence of scattering feature in the SAXS profile, which was consistent with that revealed by XRD (see the red profile in Fig. 3c) showing a sharp diffraction at 7° from the severe stacking of clay platelets due to aggregation. While for the PEG-CS/MMT-4 nanosheets, a broad scattering peak was observed at ca. $q = 2.2$ nm^{-1}, corresponding to a short-range scale length of 2.84 nm calculated using $d = 2\pi/q$. This value was well consistent with that calculated by the diffraction peak appeared at 3.1° in the XRD profile of PEG-CS/MMT-4 nanosheets (see the green curve in Fig. 3c) as they were in fact obtained from the identical peak in the overlapped SAXS/XRD region, characteristic of a mean inter-clay distance equal to 2.84 nm upon intercalation of the PEG-CS adducts. Notably, the broad scattering feature of this peak observed by SAXS was mainly attributed to the kinetically-trapped effect imposed by freeze-drying on the self-organization of PEG-CS/MMT-4 nanosheets that significantly reduced the ordering of the intercalated MMT platelets, so that enhanced drug loading in this case could be achievable. As for the PEG-CS/MMT-8 nanosheets as-prepared by freeze-drying, the SAXS profile was found to exhibit a series of scattering peaks with the integral position ratios, indicating the formation of a lamellar structure. To quantitatively understand the lamellar structure organized by the freeze-dried PEG-CS/MMT-8 nanosheets, the scattering data was fitted by the paracrystalline lamellar model as shown by the red curve in Fig. 4a, and the key fitting parameters are also presented. Here, we deduced that the local stacking of two PEG-CS adducts-intercalated MMT platelets was driven by the freeze-drying process to form MMT bundles with an average thickness of 4 nm in the PEG-CS/MMT-8 nanosheets, thus forming the first level structure; furthermore, the MMT bundles and the unintercalated amorphous PEG-CS adducts could
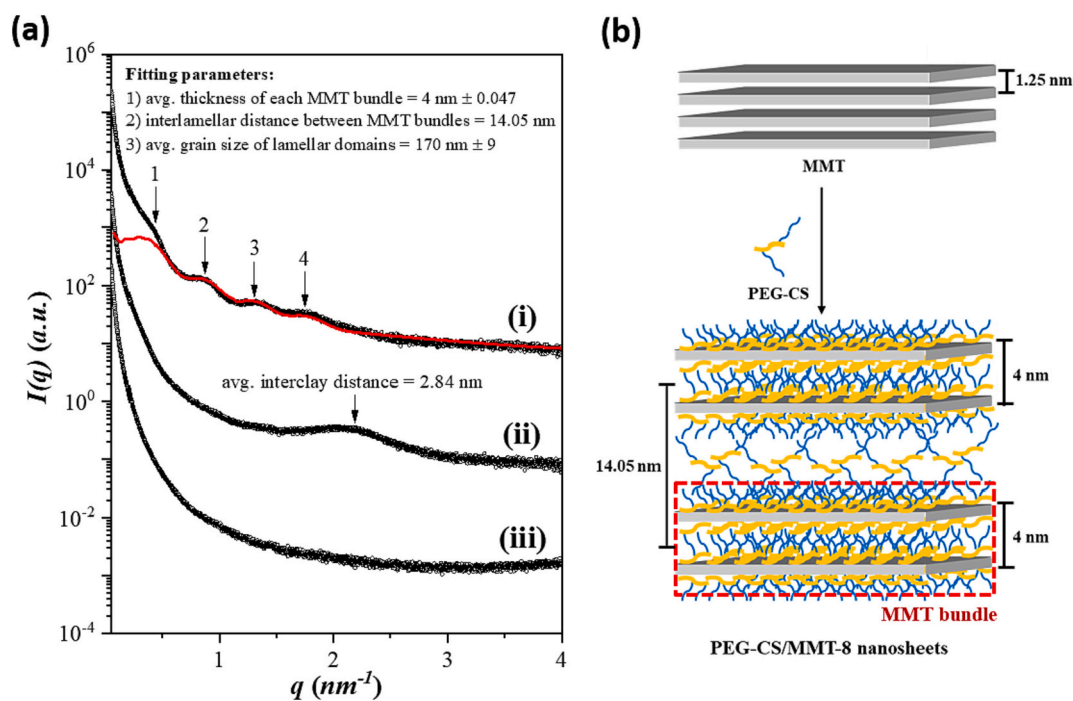
Fig. 4. (a) SAXS profiles of (i) PEG-CS/MMT-8 nanosheets, (ii) PEG-CS/MMT-4 nanosheets and (iii) MMT nanoclays. The red curve represents the fit of the experimental data by the paracrystalline lamellar model using the key parameters as listed in the figure. (b) Schematic illustration of the hierarchical structure formed in the PEG-CS/MMT-8 nanosheets. (For interpretation of the references to color in this figure legend, the reader is referred to the web version of this article.)

self-organize to construct the second level structure, where the MMT bundles were alternatingly packed by an average interlamellar distance of 14.05 nm along with the unintercalated PEG-CS domains localized in-between the MMT bundles, as schematically illustrated in Fig. 4b. Moreover, the grain size of this kind of hierarchical structure formed in the PEG-CS/MMT-8 nanosheets was up to 170 nm. The organization of MMT nanoclays and PEG-CS graft-type adducts into a hierarchical structure as observed here was firstly reported, and it shall be able to offer application potentials to the field of bio-based nanomaterials.

The complementary real-space topology of MMT nanoclays and PEG-CS/MMT nanosheets in bulk state was also investigated as displayed in Fig. 5. Prior to the real-space observation, the R_g/R_h ratio of PEG-CS/MMT-4 nanosheets dispersed in aqueous solution was determined by Berry plot using the scattering angle-dependent SLS correlation function

to evaluate the nanosheet geometry (Fig. 5a). The R_g/R_h ratio obtained for PEG-CS/MMT-4 nanosheets was ca. 1.31 (close to the value of 1.1) reported for the conventional nanosheets (Cohen et al., 1998; Hara et al., 2014), thus indicating that the MMT after being intercalated with the PEG-CS maintained a sheet-like shape. Similarly, the sheet geometry was also observed for the PEG-CS/MMT-8 nanosheets (see Fig. S2 of the Supporting Information). After confirming that the MMT nanoclays hybridizing with PEG-CS adducts could still preserve the sheet-like geometry, the real-space topology of the sheet-like PEG-CS/MMT-4 and PEG-CS/MMT-8 nanosheets was again evidenced by TEM as revealed in Fig. 5b. In addition, the SEM images in Fig. 5c showed that the particle sizes of these two PEG-CS/MMT nanosheets were both appreciably smaller than that of pristine MMT, consistent with the DLS character-ization shown in Fig. 3a. While considering that both the TEM and SEM

Fig. 5. (a) Berry plot of the correlation function versus the scattering angle to obtain the R_g/R_h ratio of PEG-CS/MMT-4 nanosheets dispersed in PBS of pH 7.4. (b) TEM micrographs of (i) MMT nanoclays, (ii) PEG-CS/MMT-4 nanosheets, (iii) PEG-CS/MMT-8 nanosheets, and (iv) DOX@PEG-CS/MMT-4 nanosheets, with scale bar of 200 nm. (c) SEM images of (i) MMT nanoclays, (ii) PEG-CS/MMT-4 nanosheets, and (iii) PEG-CS/MMT-8 nanosheets, with scale bar of 1 μm. (d) AFM height images of (i) MMT nanoclays, (ii) PEG-CS/MMT-4 nanosheets, and (iii) PEG-CS/MMT-8 nanosheets, with scale bar of 400 nm; the dashed lines marked in the images indicate the range where the thicknesses were determined.

images studied here could only show the in-plane morphology of the nanosheets, the complemented AFM images along the normal-view were further collected to link the layered topology of clay platelets to the contour morphology showing the tendency of reduced particle size with hybridization of the PEG-CS adducts. As shown in Fig. 5d, the AFM images of PEG-CS/MMT-4 and PEG-CS/MMT-8 nanosheets coated on the Si wafers showed the thicknesses of around 10–14 nm and 6–10 nm, respectively, revealing the reduction in levels of layered aggregates upon hybridization with PEG-CS adducts in comparison to the pristine MMT nanoclays with ca. 19–25 nm in thickness. It was obviously found that the formation of either the short-ranged intercalated structure in PEG-CS/MMT-4 nanosheets or the long-ranged lamellar structure organized by the alternatingly-packed intercalated MMT bundles and unintercalated amorphous PEG-CS domains in PEG-CS/MMT-8 nanosheets seemed to be favorable to reduce the thickness of the layered aggregates in the samples spin-coated for AFM study, particularly for the latter case. This was because that the more amorphous PEG-CS adducts involved in the mutual self-assembly of the PEG-CS/MMT-8 nanosheets in aqueous solution would more effectively reduce the level of aggregate after solvent removal.

### 3.2. Structural characterization of DOX@PEG-CS/MMT nanosheets

The architecture of the different PEG-CS/MMT nanosheets has been systematically investigated. In order to evaluate the feasibility of utilizing the PEG-CS/MMT nanosheets as drug vehicles, DOX was chosen as a model drug in this study. The aqueous dispersion stability of MMT nanoclays and PEG-CS/MMT nanosheets respectively loaded with DOX molecules was studied by DLS. As shown in Fig. 6a and Table 1, the DOX@PEG-CS/MMT nanosheets dispersed in PBS of pH 7.4 exhibited the D_h value of ca. 307 nm, whereas the DOX@MMT nanoclays aggregated severely into huge particles as manifested by the D_h value over 3 µm. This indicates that the functionality of stabilizing the colloidal dispersion offered by the hydrophilic PEG segments under the physiological salt concentration condition could be inherited after the PEG-CS/MMT nanosheets carried DOX molecules.

Table 1
D_h values and the drug loading characteristics of DOX@MMT nanoclays and DOX@PEG-CS/MMT nanosheets.

Sample	D_h (nm)	PDI	DLE (%)	DLC (wt %)
DOX@MMT nanoclays	3636 ± 439	0.465	88.2 ± 6.4	26.5 ± 1.9
DOX@PEG-CS/MMT-4 nanosheets	307 ± 18	0.331	77.5 ± 2.8	6.8 ± 0.3
DOX@PEG-CS/MMT-8 nanosheets	308 ± 6	0.355	27.8 ± 2.3	1.9 ± 0.2

In bulk state, the DOX@MMT nanoclays (prepared for comparison with the case of DOX@PEG-CS/MMT nanosheets) showed two diffraction peaks at 3.7° and 6.9° (see Fig. 6b), which were associated with the expanded inter-clay distance (=2.39 nm, calculated by the first-order peak at 3.7°) between MMT platelets upon intercalation by the DOX molecules, as the weak base in DOX molecules could be interacted with the clay surfaces by ionic exchange and/or directly adsorption via electrostatic attraction (Obireddy et al., 2021). As further revealed in Fig. 6b, the expansion of inter-clay spacing was more pronounced in the bulk condition of DOX@PEG-CS/MMT-4 nanosheets as indicated by a significant shift of the diffraction peak to 2.6° (which located at the peak position lower than that (=3.2°) of PEG-CS/MMT-4 nanosheets without carrying DOX, see Fig. 3c), corresponding to a larger inter-clay distance of 3.34 nm. By contrast, no obvious characteristic diffraction peak was observed for the bulk DOX@PEG-CS/MMT-8 nanosheets, suggesting that the load of DOX significantly perturbed the construction of the initially observable lamellar structure in the PEG-CS/MMT-8 nanosheets (probably caused by an excess of total incorporated molecules of the DOX drug and PEG-CS adducts in this case) and hence gave rise to the exfoliation of MMT nanoclays. Meanwhile, the DOX loading efficiency was found to be reduced remarkably from 77.5 to 27.8 % when the drug vehicle system changed from PEG-CS/MMT-4 to PEG-CS/MMT-8 nanosheets as summarized in Table 1. Indeed, as schematically illustrated in Fig. 6c, the exfoliated morphology of the DOX@PEG-CS/MMT-
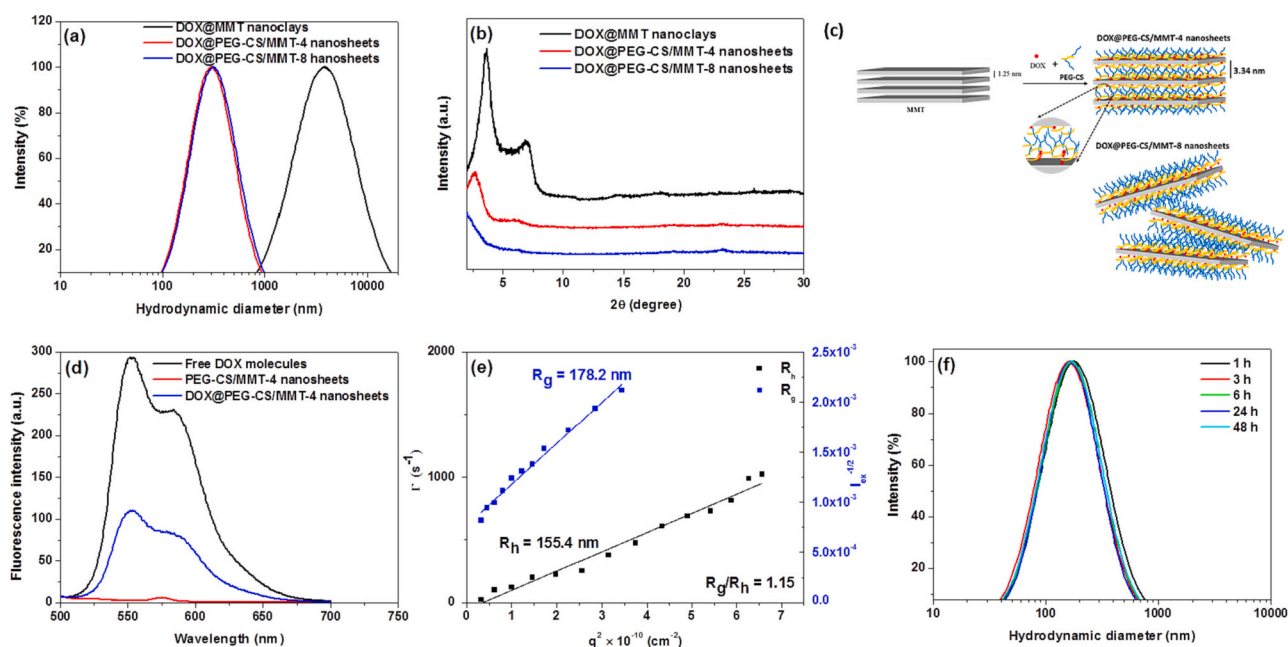
Fig. 6. (a) DLS profiles of the DOX@MMT nanoclays and DOX@PEG-CS/MMT nanosheets dispersed in PBS of pH 7.4. (b) XRD patterns of the DOX@MMT nanoclays and DOX@PEG-CS/MMT nanosheets in bulk state. (c) Schematic illustration of the microstructures of DOX@PEG-CS/MMT nanosheets. (d) Fluorescence spectra of the free DOX molecules, PEG-CS/MMT-4 nanosheets, and DOX@PEG-CS/MMT-4 nanosheets dispersed in PBS of pH 7.4. (e) Berry plot of the correlation function versus the scattering angle to obtain the R_g/R_h ratio of DOX@PEG-CS/MMT-4 nanosheets dispersed in PBS of pH 7.4. (f) DLS profiles of DOX@PEG-CS/MMT-4 nanosheets dispersed in 10 % FBS-containing PBS collected at different time intervals.

8 nanosheets greatly increased the probability of the exposure of clay-carrying DOX molecules to the surrounding aqueous phase and therefore easily facilitated the detachment of DOX molecules during purification. The other possible scenario was that the negatively-charged sites on MMT surfaces have been greatly occupied by the abundant of PEG-CS adducts in the PEG-CS/MMT-8 nanosheets, such that no more space was available for coordination with the positively-charged DOX molecules.

Let us focus on the DOX@PEG-CS/MMT-4 nanosheet system with a brief summary on its structure-directing properties, considering the better capability of carrying DOX molecules in this system. As shown in Fig. 6d, the DOX@PEG-CS/MMT-4 nanosheets displayed a considerably lower fluorescence intensity relative to the free DOX molecules at the same DOX concentration, due to the fact that most of DOX molecules were able to be localized within the inter-clay region of the PEG-CS/MMT-4 nanosheets, thereby inevitably led to a remarkable fluorescence quenching of DOX molecules at high local concentration (Elbialy & Mohamed, 2020; Lin et al., 2018). It is noted that the DOX@PEG-CS/MMT-4 nanosheets indeed still kept a sheet-like geometry (their R_g/R_h ratio in PBS solution was determined to be 1.15, as shown in Fig. 6e), similar to the drug-free PEG-CS/MMT-4 nanosheets. In brief, the good dispersity of PEG-CS/MMT-4 nanosheets was preserved for the DOX@PEG-CS/MMT-4 nanosheets even after completely removing the PBS solvent as can be identified by the TEM image shown in Fig. 5b (iv), and this vehicle system showed the highest drug loading capacity in this study. We have also carried out the time-resolved DLS experiment on the dispersion of DOX@PEG-CS/MMT-4 nanosheets in 10 % FBS-containing PBS solution and found that the D_h value of nanosheets could remain unchanged for at least 48 h (Fig. 6f), illustrating their prominent colloidal stability in the aid of surface decoration by the hydrophilic PEG.

3.3. In vitro drug release of DOX@PEG-CS/MMT nanosheets

To assess the effect of the intercalation of PEG-CS adducts into MMT nanoclay galleries on the drug release performance of DOX, the in vitro DOX dissolution test of DOX@PEG-CS/MMT-4 nanosheets (and also tests for DOX@MMT nanoclays and free DOX molecules for comparison) in aqueous solutions of pH 7.4 and 5.0 was conducted using dialysis method. As shown in Fig. 7a, compared to the fast outflow of free DOX molecules across the dialysis tube (>70 % of cumulative DOX release after 6 h), the DOX release from DOX@MMT nanoclays or DOX@PEG-CS/MMT-4 nanosheets was appreciably hindered as a consequence of the reduced diffusion kinetics of DOX molecules through the MMT galleries by their electrostatic attraction. It was further shown that

DOX@MMT nanoclays and DOX@PEG-CS/MMT-4 nanosheets exhibited a similar drug release behavior at pH 7.4, whereas at pH 5.0 the latter one displayed the faster drug liberation than the former one. On the basis of the predominant electrostatic interaction of PEG-CS adducts with the MMT nanoclays in acidic solutions, it can be speculated that at pH 5.0, the ability of association with the negatively-charged MMT surfaces by the protonated chitosan backbone from PEG-CS outweighed that by the protonated DOX molecules; as a result, the existence of PEG-CS adducts (i.e., in the DOX@PEG-CS/MMT-4 nanosheets) could impair the association of DOX molecules with MMT and simultaneously speeded up the DOX drug release when comparing to the case of DOX@MMT nanoclays.

Interestingly, when the DOX@PEG-CS/MMT-4 nanosheets were dispersed in PBS of pH 7.4 containing the 10 mM GSH for 24 h, the DOX fluorescence intensity was obviously increased by at least 1.64-fold as indicated in Fig. 7b. Contrarily, in the absence of GSH, only 1.35-fold increase in the DOX fluorescence intensity of DOX@PEG-CS/MMT-4 nanosheets in pH 7.4 PBS was attained after dispersion for 24 h. Namely, the presence of GSH promoted the DOX release more efficiently. Based on the previous study by Choi's group that the GSH molecules can be intercalated into MMT upon cation exchange (Baeka et al., 2012), a simple exchange process of GSH molecules with the intercalated DOX species could be accessible to assist the DOX liberation from nanosheets as observed in our study. The findings implied that the DOX@PEG-CS/MMT-4 nanosheets internalized by cancer cells would be able to release drug progressively in the GSH-rich (GSH concentration = 2–10 mM) and acidic intracellular milieu, thereby promoting translocation of DOX into nuclei to kill cancer cells.

3.4. In vitro cellular uptake and cytotoxicity of DOX@PEG-CS/MMT nanosheets

The cellular uptake of DOX@PEG-CS/MMT-4 nanosheets by TRAMP-C1 cells was observed by CLSM. As revealed in Fig. 8a and b, the DOX fluorescence signals recorded after the TRAMP-C1 cells have been incubated with DOX@PEG-CS/MMT-4 nanosheets at 37 °C for 1 h was clearly lower than that of cells treated with free DOX molecules. In this case, a considerable amount of free DOX molecules has been transported into the nuclei of TRAMP-C1 cells, while the amount of DOX delivered into cytoplasm by the DOX@PEG-CS/MMT-4 nanosheets was relatively small. This was primarily ascribed to the different routes of cellular internalization. Previous study has shown that free DOX molecules can rapidly penetrate cell membranes to accumulate within nuclei via the passive diffusion pathway (Hung et al., 2022; Zhang et al., 2016);
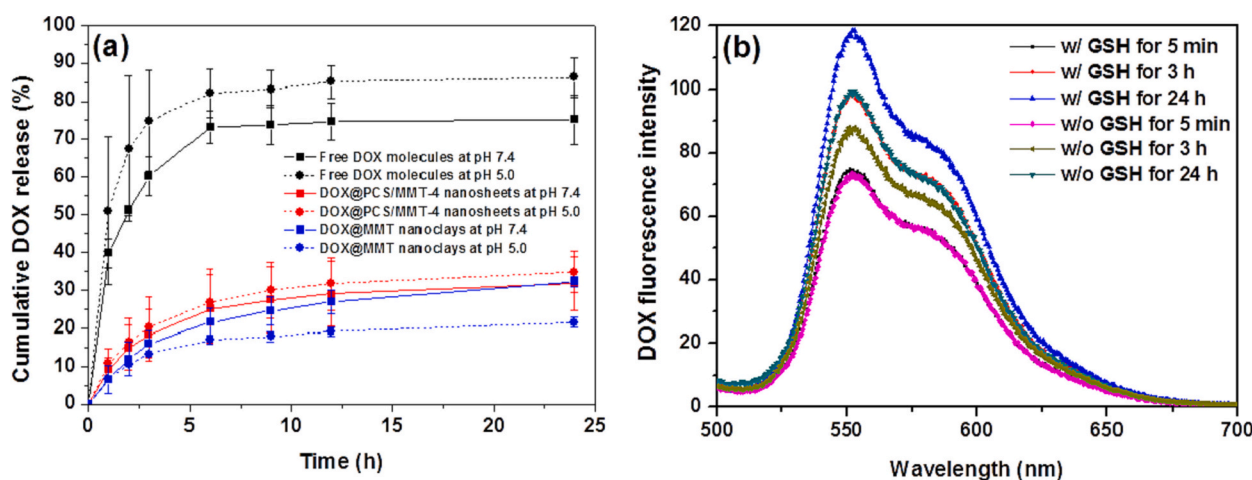

Fig. 7. (a) Cumulative DOX release profiles of the DOX@PEG-CS/MMT-4 nanosheets in aqueous solutions of pH 7.4 and 5.0. For comparison, transports of DOX@MMT nanoclays and free DOX molecules across the dialysis membrane at the same conditions are also studied. (b) Fluorescence spectra of DOX@PEG-CS/MMT-4 nanosheets dispersed in PBS of pH 7.4 containing the 10 mM GSH or not collected at different time intervals.
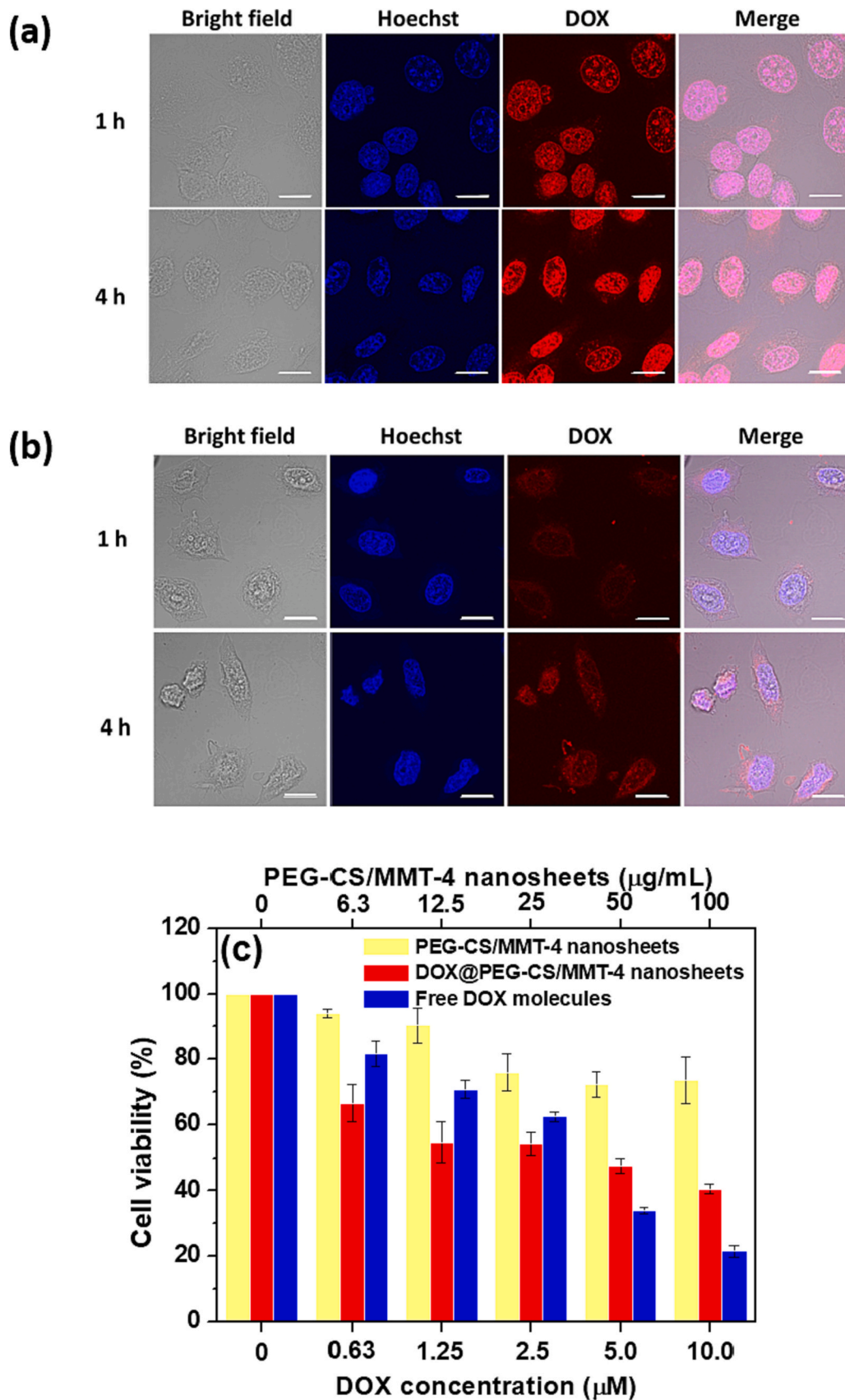
Fig. 8. CLSM images of TRAMP-C1 cells incubated respectively with (a) free DOX molecules and (b) DOX@PEG-CS/MMT nanosheets for 1 and 4 h. (c) Viability of TRAMP-C1 cells incubated with free DOX molecules, PEG-CS/MMT nanosheets, and DOX@PEG-CS/MMT nanosheets, respectively, for 24 h.

however, as presented in Scheme 1a, the DOX@PEG-CS/MMT-4 nanosheets could be progressively internalized by cells via the endocytosis pathway. For instance, when the incubation time of TRAMP-C1 cells with DOX@PEG-CS/MMT-4 nanosheets was prolonged from 1 to 4 h as shown in Fig. 8b, the DOX fluorescence intensity of cell cytoplasm and nuclei was slightly enhanced, illustrating that the cellular uptake of DOX@PEG-CS/MMT-4 nanosheets and the intracellular DOX release were progressively promoted over time. In agreement with the in vitro release study (Fig. 7), the progressive release of DOX molecules from the endocytosed DOX@PEG-CS/MMT-4 nanosheets was most probably due to the acidity/GSH-triggered responses, thus leading to a gradual deposition in the nuclei.

To further assess the anticancer effect of DOX@PEG-CS/MMT-4 nanosheets, their cytotoxicity against TRAMP-C1 cells was evaluated by MTT assay. As an important control, the high viability of TRAMP-C1 cells incubated with PEG-CS/MMT-4 nanosheets in the concentration range of 6.3 to 100 μg/mL for 24 h was attainable as indicated in Fig. 8c, indicative of only the slight toxicity of PEG-CS/MMT nanohybrids to the TRAMP-C1 cells. However, when TRAMP-C1 cells were treated with either the free DOX molecules or the DOX@PEG-CS/MMT-4 nanosheets, the cell viability was reduced in a drug concentration-dependent manner (Fig. 8c), which revealed the DOX-mediated anticancer activity. On the other hand, the IC_{50} (at ca. 4.75 μM) of DOX@PEG-CS/MMT-4 nanosheets was somewhat higher than that (at ca. 3.15 μM) of free DOX molecules, signaling the time-dependent cellular uptake behavior of DOX@PEG-CS/MMT-4 nanosheets (see Fig. 8a) and their slow in vitro drug release in the acidic environment (see Fig. 7a) that may thus lead to a time-consuming drug deposition in cell nuclei. It is worth mentioning that the cytotoxicity of DOX@PEG-CS/MMT on the normal cells may be unavoidable via non-selective endocytosis; however, it could be accessible to make the process towards eliminating harm in normal cells as much as possible, due to the fact that DOX@PEG-CS/MMT-4 nanosheets were highly expected to be accumulated in tumor sites effectively by the EPR effect. In this case, the DOX@PEG-CS/MMT-4 nanosheets could be properly internalized by tumor cells for intracellular drug release with a reduction in side effects on the normal tissues for achieving the desirable chemotherapy.

4. Conclusions

To improve the dispersion stability of MMT nanoclays for the utilization as drug vehicles under physiological condition, the graft-type PEG-CS adducts were synthesized as not only the intercalator but also the stabilizer for MMT dispersion. The PEG-CS adducts could be adsorbed on the clay surfaces and/or intercalated into the clay galleries of MMT through electrostatic attraction between the positive NH^{3+} groups of chitosan and the negatively charged sites of MMT. The resulting PEG-CS/MMT nanosheets were characterized to exhibit the PEG-rich surfaces for retaining outstanding dispersion stability in serum-containing aqueous solutions of high salt concentration. With increasing the mass ratio of PEG-CS to MMT in feed, the D_h value of PEG-CS/MMT nanosheets was appreciably reduced with forming the microstructure changing from multilayered structure to exfoliated platelets. Interestingly, the SAXS characterization showed that the PEG-CS/MMT-8 nanosheets in freeze-dried state could form the lamellar structure by the alternating packing of intercalated MMT bundles and unintercalated amorphous PEG-CS domains. However, the highest drug load capacity of DOX was attained in the PEG-CS/MMT-4 nanosheets by the multilayered structure, in which the presence of PEG-CS adducts could partly enhance the efficiency of DOX release under weak acidic condition by the protonated CS segments as compared to the case of DOX@MMT nanoclays. Additionally, the progressive liberation of drug within acidic organelles to elicit apoptosis of cancer cells after the endocytosis of DOX@PEG-CS/MMT nanosheets by TRAMP-C1 cells has been demonstrated by the in vitro cellular uptake and cytotoxicity studies. Overall, this work proposed a new strategy to develop the functionalized MMT nanoclays as

drug delivery systems.

CRediT authorship contribution statement

Hsuan-Jung Huang: Conceptualization, Methodology, Investigation, Formal analysis. **Shih-Yu Huang:** Investigation, Validation, Resources. **Tzu-Hao Wang:** Investigation, Resources. **Tzu-Yun Lin:** Methodology, Investigation. **Nan-Ching Huang:** Methodology, Investigation. **Orion Shih:** Resources. **U-Ser Jeng:** Methodology, Resources. **Che-Yi Chu:** Investigation, Resources, Funding acquisition, Writing – original draft, Writing – review & editing. **Wen-Hsuan Chiang:** Conceptualization, Writing – original draft, Writing – review & editing, Supervision, Project administration, Funding acquisition.

Declaration of competing interest

The authors declare that they have no known competing financial interests or personal relationships that could have appeared to influence the work reported in this paper.

Data availability

Data will be made available on request.

Acknowledgements

Appendix A. Supplementary data

Supplementary data to this article can be found online at https://doi.org/10.1016/j.carbpol.2022.120390.

References

Akbal, O., Vural, T., Malekghasemi, S., Bozdoğane, B., & Denkbaş, E. B. (2018). Saponin loaded montmorillonite-human serum albumin nanocomposites as drug delivery system in colorectal cancer therapy. *Applied Clay Science, 166*, 214–222.

Alemdar, A., Güngör, N., Ece, O., & Atici, O. (2005). The rheological properties and characterization of bentonite dispersions in the presence of non-ionic polymer PEG. *Journal of Materials Science, 40*, 171–177.

Altunkaynak, F., Okur, M., & Saracoglu, N. (2022). Controlled release of paroxetine from chitosan/montmorillonite composite films. *J. Drug Deliv. Sci. Technol., 68*, Article 103099.

Anirudhan, T. S., & Parvathy, J. (2018). Novel thiolated chitosan-polyethyleneglycol blend/montmorillonite composite formulations for the oral delivery of insulin. *Bioactive Carbohydrates and Dietary Fibre, 16*, 22–29.

Baeka, M., Choy, J. H., & Choi, S. J. (2012). Montmorillonite intercalated with glutathione for antioxidant delivery: Synthesis, characterization, and bioavailability evaluation. *International Journal of Pharmaceutics, 425*, 29–34.

Bekaroğlu, M. G., Nurili, F., & İşçi, S. (2018). Montmorillonite as imaging and drug delivery agent for cancer therapy. *Applied Clay Science, 162*, 469–477.

Chen, G. J., Yen, M. C., Wang, J. M., Lin, J. J., & Chiu, H. C. (2008). Layered inorganic/enzyme nanohybrids with selectivity and structural stability upon interacting with biomolecules. *Bioconjugate Chemistry, 19*, 138–144.

Chiu, C. W., Huang, T. K., Wang, Y. C., Bryan, G., Alamani, B. G., & Lin, J. J. (2014). Intercalation strategies in clay/polymer hybrids. *Progress in Polymer Science, 39*, 443–485.

Cohen, D. E., Thurston, G. M., Chamberlin, R. A., Benedek, G. B., & Carey, M. C. (1998). Laser light scattering evidence for a common wormlike growth structure of mixed micelles in bile salt- and straight-chain detergent phosphatidylcholine aqueous systems: Relevance to the micellar structure of bile. *Biochemistry (Mosc), 37*, 14798–14814.

Dang, Y., & Guan, J. (2020). Nanoparticle-based drug delivery systems for cancer therapy. *Smart Materials in Medicine, 1*, 10–19.

de Lima, P. H. C., Tavares, A. A., de Lima Silva, S. M., de Moura, M. R., Aouada, F. A., & Grillo, R. (2022). Recent advances on nanohybrid systems constituting clay-chitosan with organic molecules-a review. *Applied Clay Science, 226*, Article 106548.

Ding, Y. F., Wei, J., Li, S., Pan, Y. T., Wang, L. H., & Wang, R. (2019). Host-guest interactions initiated supramolecular chitosan nanogels for selective intracellular drug delivery. *ACS Applied Materials & Interfaces, 11*, 28665–28670.

Elbialy, N. S., & Mohamed, N. (2020). Alginate-coated caseinate nanoparticles for doxorubicin delivery: Preparation, characterisation, and in vivo assessment. *International Journal of Biological Macromolecules, 154*, 114–122.

Grillo, R., Rosa, A. H., & Fraceto, L. F. (2014). Poly(ε-caprolactone) nanocapsules carrying the herbicide atrazine: Effect of chitosan-coating agent on physico-chemical stability and herbicide release profile. *International journal of Environmental Science and Technology, 11*, 1691–1700.

Guo, S., & Huang, L. (2011). Nanoparticles escaping RES and endosome: Challenges for siRNA delivery for cancer therapy. *Journal of Nanomaterials, 2011*, Article 742895.

Hara, E., Ueda, M., Kim, C. J., Makino, A., Hara, I., Ozeki, E., & Kimura, S. (2014). Suppressive immune response of poly-(sarcosine) chains in peptide-nanosheets in contrast to polymeric micelles. *Journal of Peptide Science, 20*, 570–577.

Hoang Thi, T. T., Pilkington, E. H., Nguyen, D. H., Lee, J. S., Park, K. D., & Truong, N. P. (2020). The importance of poly(ethylene glycol) alternatives for overcoming PEG immunogenicity in drug delivery and bioconjugation. *Polymers, 12*, 298.

Hsieh, M. H., Wang, T. H., Hu, S. H., Hsu, T. C., Yow, J. L., Tzang, B. S., & Chiang, W. H. (2022). Tumor site-specific PEG detachment and active tumor homing of therapeutic PEGylated chitosan/folate-decorated polydopamine nanoparticles to augment antitumor efficacy of photothermal/chemo combination therapy. *Chemical Engineering Journal, 446*, Article 137243.

Hsu, C. W., Hsieh, M. H., Xiao, M. C., Chou, Y. H., Wang, T. H., & Chiang, W. H. (2020). pH-responsive polymeric micelles self-assembled from benzoic-imine-containing alkyl-modified PEGylated chitosan for delivery of amphiphilic drugs. *International Journal of Biological Macromolecules, 163*, 1106–1116.

Huang, S. J., Wang, T. H., Chou, Y. H., Wang, H. M., Hsu, T. C., Yow, J. L., Tzang, B. S., & Chiang, W. H. (2022). Hybrid PEGylated chitosan/PLGA nanoparticles designed as pH-responsive vehicles to promote intracellular drug delivery and cancer chemotherapy. *International Journal of Biological Macromolecules, 210*, 565–578.

Hung, Y. N., Hung, Y. N., Liu, Y. L., Chou, Y. H., Hu, S. H., Cheng, B., & Chiang, W. H. (2022). Promoted cellular uptake and intracellular cargo release of ICG/DOX-carrying hybrid polymeric nanoassemblies upon acidity-activated PEG detachment to enhance cancer photothermal/chemo combination therapy. *European Polymer Journal, 163*, Article 110944.

Iliescu, R. I., Andronescu, E., Ghitulica, C. D., Voicu, G., Ficai, A., & Hoteteu, M. (2014). Montmorillonite-alginate nanocomposite as a drug delivery system-incorporation and in vitro release of irinotecan. *International Journal of Pharmaceutics, 463*, 184–192.

Jafarbeglou, M., Abdouss, M., Shoushtari, A. M., & Jafarbeglou, M. (2016). Clay nanocomposites as engineered drug delivery systems. *RSC Advances, 6*, 50002–50016.

Jermy, B. R., Ravinayagam, V., Almohazey, D., Alamoudi, W. A., Dafalla, H., Akhtar, S., & Tanimu, G. (2022). PEGylated green halloysite/spinel ferrite nanocomposites for pH sensitive delivery of dexamethasone: A potential pulmonary drug delivery treatment option for COVID-19. *Applied Clay Science, 216*, Article 106333.

Joshi, G. V., Kevadiya, B. D., Patel, H. A., Bajaj, H. C., & Jasra, R. V. (2009). Montmorillonite as a drug delivery system: Intercalation and in vitro release of timolol maleate. *International Journal of Pharmaceutics, 374*, 53–57.

Khatoon, N., Chu, M. Q., & Zhou, C. H. (2020). Nanoclay-based drug delivery systems and their therapeutic potentials. *Journal of Materials Chemistry B, 8*, 7335–7351.

Kohay, H., Sarisozen, C., Sawant, R., Jhaveri, A., Torchilin, V. P., & Mishael, Y. G. (2017). PEG-PE/clay composite carriers for doxorubicin: Effect of composite structure on release, cell interaction and cytotoxicity. *Acta Biomaterialia, 55*, 443–454.

Lanz-Landázuri, A., de Ilarduya, A. M., García-Alvarez, M., & Sebastián Muñoz-Guerra, S. (2014). Poly(β, L-malic acid)/doxorubicin ionic complex: A pH-dependent delivery system. *Reactive and Functional Polymers, 81*, 45–53.

Lee, K. S., Chung, H. C., Im, S. A., Park, Y. H., Kim, C. S., Kim, S. B., Rha, S. Y., Lee, M. Y., & Ro, J. (2008). Multicenter phase II trial of genexol-PM, a cremophor-free, polymeric micelle formulation of paclitaxel, in patients with metastatic breast cancer. *Breast Cancer Research and Treatment, 108*, 241–250.

Li, Z., Ye, E., David, R., Lakshminarayanan, R., & Loh, X. J. (2016). Recent advances of using hybrid nanocarriers in remotely controlled therapeutic delivery. *Small, 12*, 4782–4806.

Lin, Y., Yang, Y., Yan, J., Chen, J., Cao, J., Pu, Y., Li, L., & He, B. (2018). Redox/ATP switchable theranostic nanoparticles for real-time fluorescence monitoring of doxorubicin delivery. *Journal of Materials Chemistry B, 6*, 2089–2103.

Manocha, B., & Margaritis, A. (2010). Controlled release of doxorubicin from doxorubicin/γ-polyglutamic acid ionic complex. *Journal of Nanomaterials, 2010*, Article 780171.

Mitchell, M. J., Billingsley, M. M., Haley, R. M., Wechsler, M. E., Peppas, N. A., & Langer, R. (2021). Engineering precision nanoparticles for drug delivery. *Nature Reviews. Drug Discovery, 20*, 101–124.

Mokhtar, A., Djelad, A., Bengueddach, A., & Sassi, M. (2018). Biopolymer-layered polysilicate micro/nanocomposite based on chitosan intercalated in magadiite. *Research on Chemical Intermediates, 44*, 6469–6478.

Monvisade, P., & Siriphannon, P. (2009). Chitosan intercalated montmorillonite: Preparation, characterization and cationic dye adsorption. *Applied Clay Science, 42*, 427–431.

Murugesan, S., & Scheibel, T. (2020). Copolymer/clay nanocomposites for biomedical applications. *Advanced Functional Materials, 30*, Article 190810.

Obireddy, S. R., Subbarao, S. M. C., Venkata, K. R. K. S., & Lai, W. F. (2021). Development and characterization of montmorillonite-based hybrid materials for pH-responsive drug delivery. *ChemistrySelect, 6*, 1466–1470.

Peixoto, D., Pereira, I., Pereira-Silva, M., Veiga, F., Hamblin, M. R., Lvov, Y., Liu, M., & Paiva-Santos, A. C. (2021). Emerging role of nanoclays in cancer research, diagnosis, and therapy. *Coordination Chemistry Reviews, 440*, Article 213956.

Sreekanth Reddy, O., Subha, M. C. S., Jithendra, T., Madhavi, C., & Chowdoji Rao, K. (2021). Curcumin encapsulated dual crosslinked sodium alginate/montmorillonite polymeric composite beads for controlled drug delivery. *Journal of Pharmaceutical Analysis, 11*, 191–199.

Takahashi, T., Yamada, Y., Kataoka, K., & Nagasaki, Y. (2005). Preparation of a novel PEG-clay hybrid as a DDS material: Dispersion stability and sustained release profiles. *Journal of Controlled Release, 107*, 408–416.

Tavares, A. A., Macedo, M. D. M., de Lima, P. H. C., Barbosa, R. C., Sousa, W. J. B., Diniz, C. M. G. P., … Souza, M. F.d. (2022). Chitosan-clay nanocomposite as a drug delivery system of ibuprofen. *Res., Soc. Dev., 11*, Article e25911124684.

Yalamandala, B. N., Shen, W. T., Min, S. H., Chiang, W. H., Chang, S. J., & Hu, S. H. (2021). Advances in functional metal-organic frameworks based on-demand drug delivery systems for tumor therapeutics. *Advanced NanoBiomed Research, 1*, 2100014.

Yuan, Q., Shah, J., Hein, S., & Misra, R. D. K. (2010). Controlled and extended drug release behavior of chitosan-based nanoparticle carrier. *Acta Biomaterialia, 6*, 1140–1148.

Zhang, Y., Li, P., Pan, H., Liu, L., Ji, M., Sheng, N., Wang, C., Cai, L., & Ma, Y. (2016). Retinal-conjugated pH-sensitive micelles induce tumor senescence for boosting breast cancer chemotherapy. *Biomaterials, 83*, 219–232.